J-Integral Analysis of the Elastic Strain Fields of Ferrite Deformation Twins using Electron Backscatter Diffraction

Abdalrhaman Koko[a*], Elsiddig Elmukashfi[b], Kalin Dragnevski[b], Angus J. Wilkinson[a], and Thomas James Marrow[a]

[a] Department of Materials, University of Oxford, Oxford OX1 3PH, UK

[b] Department of Engineering Science, University of Oxford, Oxford OX1 3PJ, UK

* Corresponding authors.

E-mail address: abdo.koko@materials.ox.ac.uk

Abstract

The strain fields of deformation twins in the ferrite matrix of an age-hardened duplex stainless-steel (Zeron 100: 25%Cr, 7%Ni) have been studied in situ under load, and ex situ (unloaded), using high-resolution electron backscatter diffraction (HR-EBSD). The local 2-dimensional (2D) elastic strain field acting on the twin tip was parametrised for the first time using the strain energy release rate (*J*-integral) and then decomposed into the mode I and mode II stress intensity factors (K_I and K_{II}). An improved method to select the strain reference was used, based on the relationship between the HR-EBSD cross-correlation peak height and mean angular error. The elastic field described by K_I increased with twin thickness. The in-plane shear field, described by K_{II}, relaxed when the load was removed. Some current limitations of the 2D analysis are discussed, which aims to provide an experimental methodology to quantify the fields that describe the local boundary conditions for twin thickening and propagation.

Keywords: HR-EBSD; Deformation twinning; *J*-integral; Finite element analysis; Ferrite

1. Introduction

Deformation or mechanical twinning is an important mechanism to accommodate plastic strains by crystal shape change when sufficient independent slip systems cannot be activated, for example, crystals with low-symmetry [1] or deformation at low temperature [2]. Significant attention has been paid to the crystallography [2]–[6], morphology [7]–[9] and macro mechanical effects [9]–[11] of deformation twinning. Although the criterion for deformation twin growth is not completely understood, it is a tip controlled phenomena linked to the interaction between the residual and mobile twin partials at the twin interface; thermodynamically this involves the elastic energy of the strained lattice, the interface and volume free-energy of the twin, and the dissipated energy of the growth mechanism [1], [5]. To fully understand the interactions between microstructure (i.e., grain size, texture), temperature and strain rate on deformation twinning, it is important to be able to characterise the local stress and strain field associated with twin thickening and propagation. This is especially important for materials where cleavage fracture can be initiated by twinning (e.g. iron-silicon [12] and the ferrite of age hardened duplex stainless-steel [13]).

In body-centred cubic metals, a deformation twin embryo forms by the accumulation of stacking faults, with a variant selection that is governed by the local stress state [4], [14], [15]. The twin propagates when the homogeneous shear stress reaching a critical value, and a twin-parent interface advances inside the parent grain [4]. The propagating deformation twin generates a stress field due to its confinement by the surrounding parent crystal, and deformation twins develop a 3D oblate spheroid shape (which appears in 2D sections as a bi-convex lens) with a mixed coherent and non-coherent interface (Figure 1a) [16], [17]. Elastic simulations of the local stress field surrounding the ellipsoidal twin tip find the field can be described using its lens angle (β) and that the stress field magnitude increases with twin thickness [14], [18]. In practice, plastic accommodation occurs in the parent crystal and is dependent on the material's yield stress, the anisotropic elastic stiffness of the crystal lattice, and the twinning shear magnitude [19], [20].

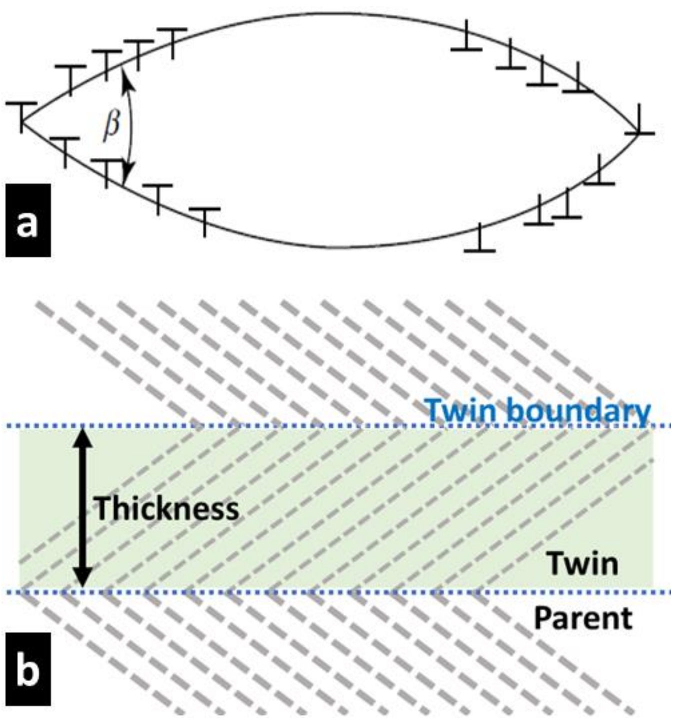

Figure 1: (a) Schematic of a lenticular twin with interface dislocations and (b) Twin band.

Deformation twin growth can be perceived as a two-step process of i) thickening that is mediated by the interaction between the residual and mobile twin partials at the coherent twin-parent interface [20], and ii) dislocation mobility along the twin shear direction [17], [19]. The corresponding stress fields can provide a sufficient driving force for concurrent twin nucleation and inter/intra-granular crack nucleation [21]. A linear variation has been observed between twin thickness, stacking fault energy [22] and grain size [6], and to a lesser degree the stress state of the twinning grain (Schmid factor) [23].

Early studies of deformation twins arrested within grains of niobium [24] and iron [25] visualised the extremely high local strain concentration at the twin tip by using an etch-pit procedure. More recently, high-resolution electron backscatter diffraction (HR-EBSD) has been used to investigate the strain ‘singularity’ ahead of a twin tip in hexagonal close-packed (HCP) zirconium alloy [26]. A deformation twin in commercial purity titanium was characterised similarly and then quantified using a local Schmid factor (LSF) at the twin tip [27], [28], as described in eq. (1),

$$\mathrm{LSF} = \frac{\sigma : S}{\|\sigma\|}, \qquad \text{Schmid matrix}\left(S_0^i\right) = d^i \otimes n^i \tag{1}$$

where $\|\sigma\|$ is the maximum principal stress, d^i is the shear direction and n^i is the plane normal for i^{th} slip system. The authors concluded that twin thickening and propagation are controlled by conditions at the twin tip, in a manner analogous to the operation of dislocation sources ahead of a crack-tip [29]. In the analysis, a broad region of high LSF ahead of the twin tip favoured propagation, whereas a narrow region of high LSF promoted thickening. It has since been argued [30] that the LSF strongly controls the twin variant selection, as twinning has strong polarity (e.g. some variants within a specific twin mode operate only in compression).

The LSF novelty – compared to other criteria to describe conditions at the twin [6], [15], [31] – lies in combining a geometrical criteria with the deformation field in the parent grain to provide an approximate indication of the local twin mode (i.e. thickening or propagation). However, the LSF analysis does not take advantage of the available full-field data, relies on global information on the applied stress, and does not consider the energy-balance that drives twin growth. To the authors' knowledge, there have been no in-situ experiments to quantify the strain field ahead of a propagating deformation twin. Such observations might be used to validate geometrical [6] or hybrid geometrical-energy based criteria [15], [29], [30] for growth. Nanoscale testing (i.e. transmission electron microscopy) may not represent the behaviour in bulk samples [32], so a suitable analysis method is needed.

Using a two-dimensional dislocation-based model for a twin within a single magnesium grain, Lloyd [33] described the stress concentration field ahead of the twin tip. Wang and Li [34], who considered microscopic phase-field (MPF) models of cracks, noted that the stress fields were similar for dislocations, deformation twinning and martensitic transformations, with differences only in the traction of the created surface; i.e. there is 100% traction recovery for dislocations and a traction-free surface for a crack. They highlighted that the stress field singularity regulates the advancement of the crack-tip and dislocations. This stress concentration can be characterised using a path independent line integral, as shown by Eshelby for dislocations with consideration of the contribution from the surface traction, and for ellipsoidal inclusions [35], [36], and by Rice [37] for cracks and stress concentrations with traction free surfaces. And, as noted by Venables [5], the oblate spheroid shape of the twin tip is the ideal example of an ellipsoid inclusion or a notch. This path independent line integral, the *J*-integral, is defined by equation (2). In the context of crack fields, it is obtained by formulating a contour or domain independent integral (Figure 2) that starts from the free surface of the crack tip to calculate the elastic energy release rate in the direction of a virtual crack extension [38].

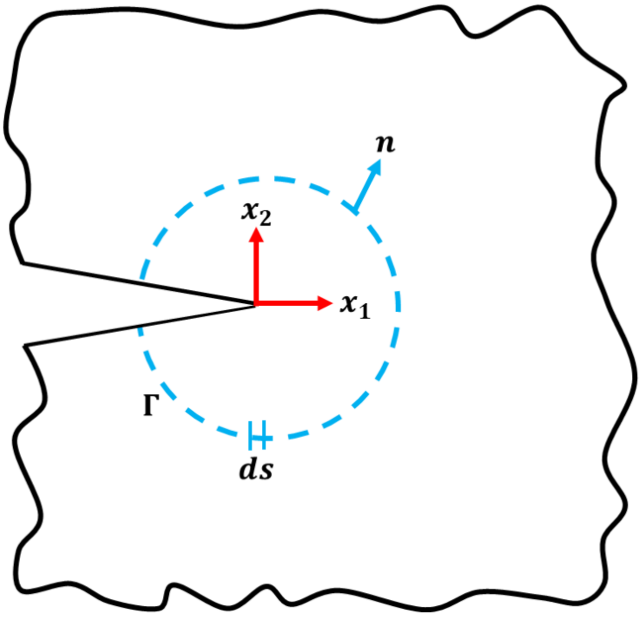

Figure 2: An arbitrary contour (Γ) enclose a crack tip's deformation field.

$$J = \int_{\Gamma} \left(W dx_2 - T_i \frac{\partial u_i}{\partial x_1} ds \right), \qquad W = \int_0^{\varepsilon_{ij}} \sigma_{ij} d\epsilon_{ij}, \qquad T_i = \sigma_{ij} n_j, \tag{2}$$

where σ_{ij} and ϵ_{ij} are the stress and strain tensors, respectively, W is the strain energy density, T_i are the components of the traction vector, u_i are the displacement vector components, n_j are the components of the unit vector normal to Γ and ds is the length increment along the contour Γ. In fracture studies, it has been shown that the *J*-integral can be evaluated from experimental full-field measurements of the crack tip displacement [39], [40] or elastic strain field [41]–[43]. For conditions of small-scale yielding, the J-integral can be decomposed into the elastic stress intensity factors (K_I, K_{II} and K_{III}), by use of the interaction integral [44], to describe the opening, in-plane shear and out-of-plane shear of the stress concentration [45].

Previous analyses that used HR-EBSD to measure the strain field ahead of blocked slip-bands [46]–[48] and deformation twins [49] have demonstrated their singularity-like behaviour. Here, we have applied a full-field 2-dimensional *J*-integral analysis and the interaction integral to HR-EBSD data for the first time to quantitatively characterise the mechanical conditions surrounding the tips of intragranular twins. Our objective is to ultimately develop an experimental methodology to investigate the criteria for twin growth and the mechanical interactions between twins and other microstructure features (twins, grain boundaries, precipitates), which affect the plasticity and fracture of polycrystalline metals.

The paper is structured as follows: Following a brief description of the experimental methodology, the analysis of the J-integral from HR-EBSD data is presented as it is applied to an intragranular twin in a ferrite grain that is observed as the twin thickens and extends when the applied tensile strain is increased. The full details of the selection of the HR-EBSD reference pattern and the trace analysis to characterise twins and slip bands are provided in the supplementary information. Ex situ analyses of several ferrite twins are then presented to examine the characteristic stress intensity factors K_I and K_{II} of the elastic fields around unloaded twins. The limitations of the current 2D analysis are discussed.

2. Methodology

The material sample was from a large (~200 mm thickness) forging of Zeron 100 duplex stainless steel (DSS) with a nominal composition of 25% Cr, 7% Ni, 3.6% Mo, 0.7% Cu, 0.7% W, 0.22% N. Duplex stainless steel was selected as it is a well characterised material in which slip band and twin formation in the coarse-grained ferrite can be encouraged during slow strain rate, room temperature deformation, through age-hardening without any other change in microstructure [50], [51]. It is also a suitable model material for EBSD analysis as the polished surface does not oxidise further, and high-quality patterns can be acquired in a reasonable time. Specimens for both in situ and ex situ study were prepared with a dog-bone geometry (nominally 30×14×1.5 mm^3), as shown in Figure 3, before being aged in air at 475°C for 100 hrs to cause age-hardening of the ferrite by spinodal decomposition. This encourages ∑3 {211}<111> ferrite deformation twinning at room temperature, with no significant change in the austenite properties [51], [52]. The observed surface of the aged specimens was ground using SiC papers from 240 to 4000 grit, and polished using diamond paste (from 9 to 1 µm), finishing with 50 nm colloidal silica for 2 hours (50 rpm speed and 5 N force) to produce a mirror-flat surface without artefacts. The specimens were ultrasonically cleaned for 20 minutes using ethanol, rinsed with deionised water, and dried with a hot air blower.

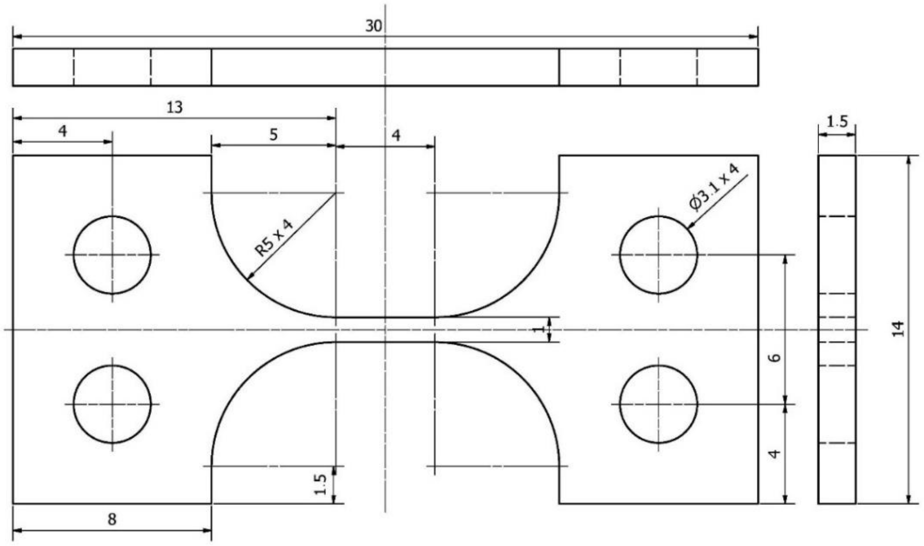

Figure 3: Zeron 100 duplex stainless-steel tensile specimen (dimensions in mm).

The specimens were loaded using a 70° pre-tilted 2 kN Tensile Deben® stage, in a Carl Zeiss Merlin FEG-SEM system equipped with Bruker e-flash high resolution EBSD detector. Before observations were made, both the stage and specimen were plasma cleaned within the microscope for 4.5 hours (3 cycles of 45 minutes plasma cleaning followed by purging). The deformation was performed in tension using a motor speed of 0.1 mm/min. For the in situ test, the nominal engineering stress and strain were evaluated using the tensile load and initial cross-section dimension, and the change in crosshead displacement for the nominal gauge length of 4 mm.

The in situ specimen was observed using both secondary electron (SE) and forescatter diode (FSD) imaging, until a suitable region of interest (ROI) was identified for higher resolution analysis. Arrays of electron backscatter diffraction patterns (EBSPs) were then collected to map the ROI at increasing levels of applied nominal strain. Before each observation, the setup was left to stabilise for 30 minutes at fixed crosshead displacement. The microscope conditions were 10 nA/20 keV beam current/voltage and 18 mm working distance. The collected high quality EBSPs were recorded as an 800 × 600 pixel map, with 100 milli-second exposure time per pattern, 4 × 4 pattern binning, and step size of 75 nm. These conditions provided a practical time for measurement (75 minutes for 18.6 × 14 μm^2 map) while avoiding sample drift [53], [54]. The same conditions were used to analyse regions of interest in the ex situ specimen, after unloading, that were selected by survey of the deformed gauge length region using FSD and secondary electron imaging.

3. Results

3.1. In Situ Tensile Test: Region of Interest Selection

The nominal applied stress and strain of the in-situ test specimen are presented in Figure 4a. Plasticity occurred with planar slip in the austenite phase, and deformation twinning in the ferrite (Figure 4b). The average stress relaxation during each 30 minutes stabilising period, which occurred mainly at the start, was 54 MPa, and was negligible (average 0.44 MPa) during HR-EBSD mapping of the region of interest (ROI). The subsequent analysis considers data obtained at nominal strains of 15, 20 and 22%.

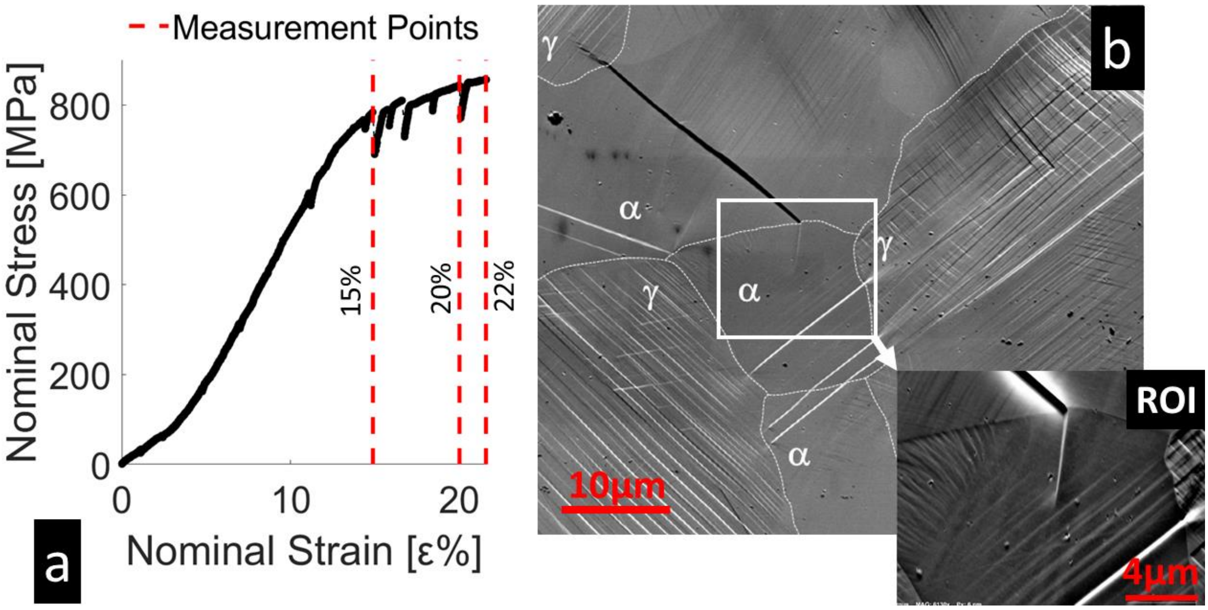

Figure 4: a) Nominal stress-strain curve for DSS sample deformed in tension and observed in situ. Stress relaxation occurred during the hold before each HR-EBSD measurement, and the highlighted points (dashed red lines) show the strains at which HR-EBSD measurements were analysed; b) secondary electron (SE) image to show the Region of Interest (ROI) and a forescatter diode (FSD) close-up taken at 15% nominal strain with white dotted grain boundaries.

The selected ROI contains a linear feature that is blocked by $\sum 3$ {60°} ferrite-ferrite grain boundary (Figure 5a) (The two grains will be designated α,1 and α,2). There is no change in crystal orientation across the linear feature, and it is identified by trace analysis as a $(121)[1\bar{1}1]$ slip-band. The Luster and Morris [55] m' parameter for the blocking ferrite-ferrite grain boundary is ~1, which indicates a '*soft*' boundary that can accommodate slip transfer. However, this criteria is only relevant for the statistical analysis of slip-to-slip transfer [56] and it has no reported association with slip-to-microcrack transfer [57] and, in this instance, slip-to-twin transfer. The slip band is predicted to have a 0.30 Schmid factor due to the applied tensile stress. From a Taylorian point of view [58], [59], the single grain response to the global boundary conditions (i.e. uniaxial tensile) is complicated in polycrystalline materials by the constraints that are imposed by the neighbouring crystals, so this Schmid factor may not necessarily represent the true local stress state.

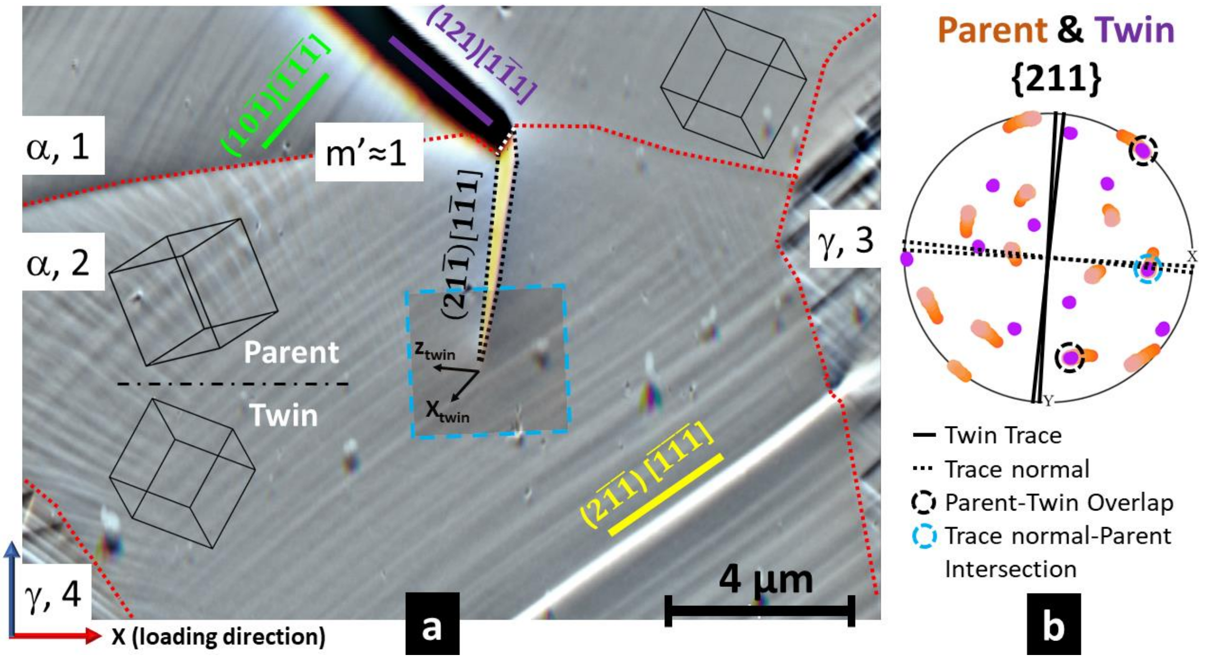

Figure 5: a) Forescatter diode (FSD) image for the ROI, at 22% nominal strain, with grain boundaries delineated with red dots, purple green and yellow lines define the slip-band traces, and dotted black lines outline the twin interfaces. The crystal unit cell orientation for the parent, twin and neighbouring ferrite grains are superimposed. b) Stereographic projection pole figure for {211} in the parent and twin of ferrite grain (α,2), with traces of the twin/parent interface (i.e. twin invariant plane) shown by black solid lines and the planes containing the poles of the interfaces shown by dotted solid lines. The normal to the identified twin invariant plane is circled (pale blue).

A deformation twin developed in the ferrite grain (α,2) at the head of the blocked slip band that is in the other ferrite grain (α,1). EBSD analysis confirmed its 60° misorientation to the parent grain, and from trace analysis (see supplementary information: C), this is judged to be a ∑3 twin of the $(21\bar{1})[1\bar{1}1]$ variant, with the pole of its twin invariant plane inclined at 56 ± 2° to the surface normal. The projection on the specimen surface of the twin shear direction in the twin invariant plane is at 48° to the loading direction (X_{twin} in Figure 5a, where Z_{twin} is the projection of the twin plane normal [27]). By a similar analysis, the slip traces that are visible in grains α,1 and α,2 are $(10\bar{1})[\bar{1}\bar{1}\bar{1}]$ with 0.47 Schmid factor (green line), and $(2\bar{1}\bar{1})[\bar{1}\bar{1}\bar{1}]$ with 0.48 Schmid factor (yellow line), respectively.

3.2. In Situ Tensile Test: Twin Surface Length and Width

To determine whether twin thickness and length changed with the increase in applied strain, which would indicate twin thickening and propagation in equilibrium with the surrounding field, the surface widths of the $(21\bar{1})[1\bar{1}1]$ twin and $(121)[1\bar{1}1]$ slip band (purple line in Figure 5a) were measured near the ferrite/ferrite grain boundary (dotted white line Figure 5b) and normal to the slip band's apparent edges, respectively. Repeat measurements (at least 5 times) were made manually using the ImageJ [60] and the results were averaged (Figure 6c). A novel edge-detection method was used to measure the twin length in an objective manner. After alignment of the FSD images (pixel size 6 nm) with an efficient Fourier-space subpixel image registration algorithm [43], and cropping and rotating the region of interest (blue dashed square in Figure 5a), the images (Figure 6a) were interpolated to fill the few points with no data (NaN). A median filter was applied to reduce noise, before mapping the phase congruency of the image intensity. Phase congruency [61], [62] is contrast invariant and identifies where the Fourier components of the image are most in phase, such as edges. The phase congruency map was threshold segmented to obtain a binary image that identified the regions of high phase congruency, and its Hough transform used to detect and measure the largest linear feature (i.e. the deformation twin) (Figure 6b). The slip band surface width, twin length and twin surface width increased with the applied strain (Figure 6c) by up to 450 nm, 60 nm and 335 nm, respectively. At the initial observation of 15% strain, the slip band width was 0.51 ± 0.01 µm, whereas the twin had a length of 5.63 ± 0.01 µm and a width of 0.4 ± 0.01 µm.

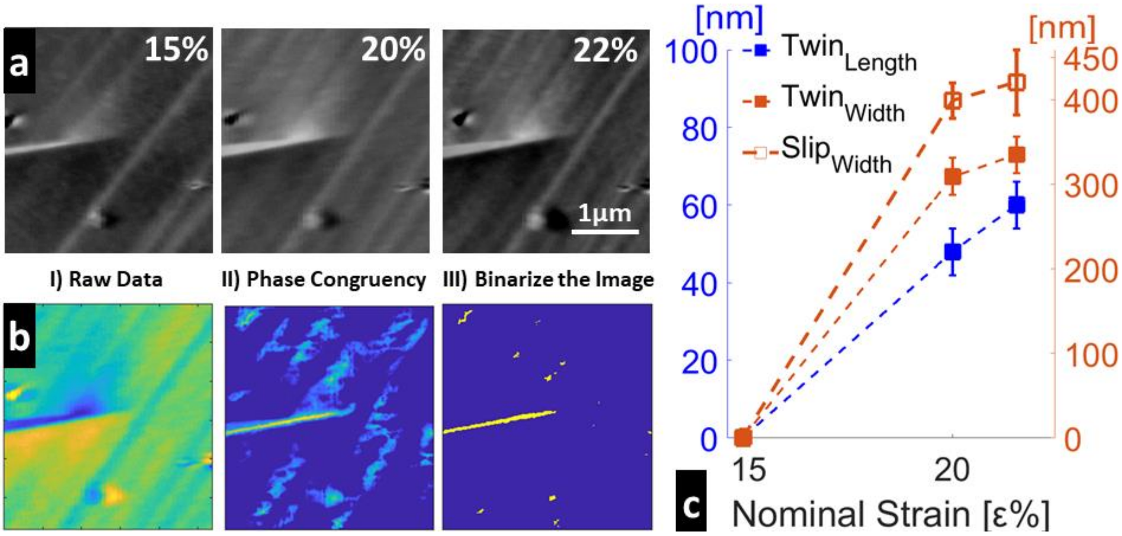

Figure 6: (a) FSD images of the ROI with increasing applied nominal strain. (b) Post-processing (false colour image intensity) to segment the twin from the FSD image using phase congruency (example at 15% nominal strain). (c) The change in slip band width, twin width, and twin length (the variance is the measurement resolution) with strain, relative to the initial observation at 15% nominal strain.

3.3. HR-EBSD Analysis

The EBSD pattern (EBSP) is affected by deformation, since elastic strains change the crystal lattice spacing and thus the Kikuchi band width. Strain also changes interplanar angles (shift of the zone axis) and can blur the EBSP due to the intense rotation gradients in the crystal that are caused by dislocations [63]. However, conventional EBSD analysis (e.g. [64]) is too insensitive to quantify the elastic deformation and plasticity, which can be partially represented by the density of geometrically necessary dislocations (i.e. GND) [65].

High (angular) resolution electron backscatter diffraction (HR-EBSD) [66], [67] utilises cross-correlation to precisely measure the deformation of the EBSPs within each grain relative to a reference pattern (EBSP$_0$) [68]. The analysis relates the difference in interplanar angles and lattice rotations to the displacement gradient tensor (F^e), which is solved to quantify the relative deformation gradient tensor (e_{ij}) within each grain. This deformation tensor is composed of elastic strains (symmetric part), ϵ_{ij}, and lattice rotations (asymmetric part), ω_{ij}. In this work, the analysis was performed iteratively to minimise strain errors due to large misorientations (>1.5°); in the second pass the EBSPs were remapped to an orientation close to EBSP$_o$ by using a local rotation matrix that is estimated from the first pass [69].

The HR-EBSD analysis finds only the elastic components of deformation (deviatoric strain and lattice rotation) and does not measure the hydrostatic strain, which changes only the width of the Kikuchi bands and not interplanar angles [70]. However, by imposing suitable boundary conditions (i.e. the stress normal to the surface is zero) and using the crystal elastic constants [71], [72], the full three-dimensional strain and stress tensors in the observed surface layer can be accessed. In this analysis, the ferrite elastic constants (in GPa) were: $C_{11} = 230, C_{44} = 117, C_{12} = 135$ [73]. The pattern centre (PC) shift due to beam movement during acquisition was corrected using the code AstroEBSD [74]. No further angular effect from drift was expected as the ROI was very small and the sample was conductive [72]. The number density of geometrically necessary dislocations (GND) was estimated from the local lattice curvature; the method used ideas based on Sun et al. [75] and El-Dasher et al. [76], implemented by Wilkinson and Randman [53] with a more complete description of the rotation gradient that retains six measured terms.

In the analysis of the in situ experiment, the chosen reference $EBSP_0$ (i.e. pattern with least deformation) was taken from the 1st ROI observation at the nominal applied strain of 15% (see Supplementary Information A for the method). This same pattern was then used as the reference for the subsequent observations, which were obtained under the same conditions without interruption or stage movement (see Supplementary Information E for comparison). Maps of the in-plane components of the calculated elastic strain tensors ($\varepsilon_{xx}, \varepsilon_{yy}$ and ε_{xy}) are presented in Figure 7 for the three observations at 15%, 20% and 22% nominal applied strain, together with maps of the GND.

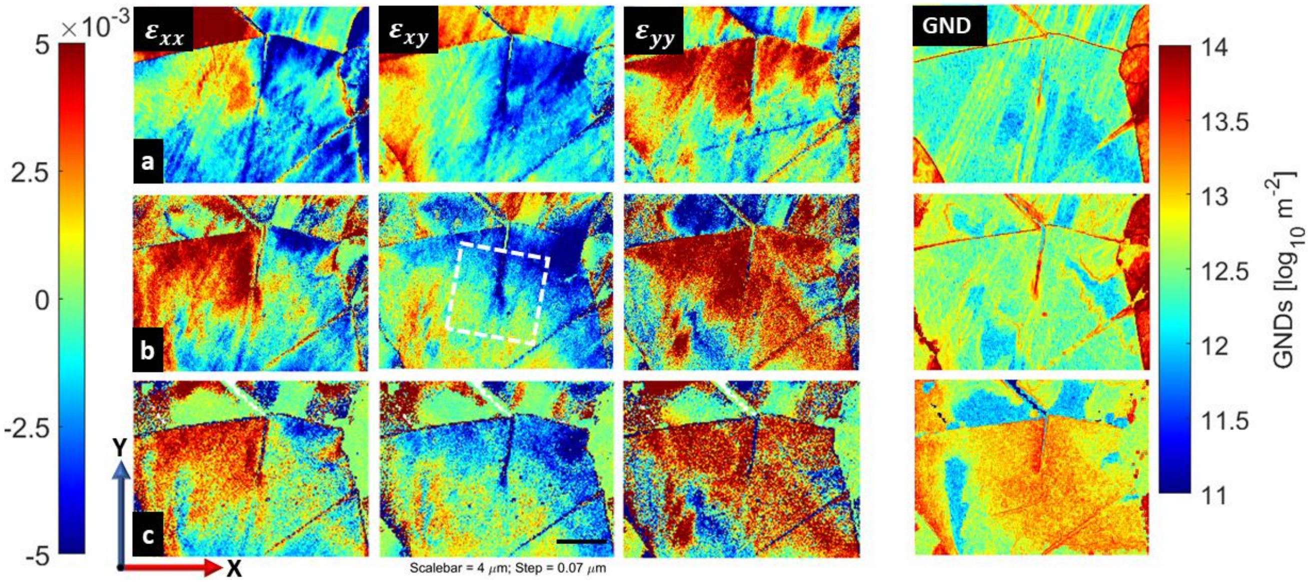

Figure 7: Maps of the in-plane components of the elastic strain tensors (ε_{xx}, ε_{yy} and ε_{xy}) and GND in the ROI, calculated using HR-EBSD at applied nominal strains of a) 15%, b) 20% and c) 22%.

The effect of applied strain on the average stress (parallel and perpendicular to the applied loading) in grain (α,2) was investigated. First, the mapped strain field was censored to exclude points that were close to strain concentrations using GND density, i.e. four iterations of removing points with GND density higher than the iteration's; the remaining points that comprised 4% of the 33,178 measurement points in each map (Figure 8a) with an average MAE of 3.5 x 10^{-4}, 3.4 x 10^{-4}, and 3.2 x 10^{-4}, and PH of 0.74, 0.70 and 0.84 at 15%, 20%, and 22% nominal strain, respectively. The statistical distributions of stress, parallel (σ_{xx}) and perpendicular (σ_{yy}) to the direction of loading, are presented in Figure 8b as a function of the nominal applied strain. The data, which describe the stresses relative to the reference pattern, are quite scattered. Nonetheless, the mean parallel stress increased with applied nominal strain, whereas there was no significant change in the perpendicular stress.

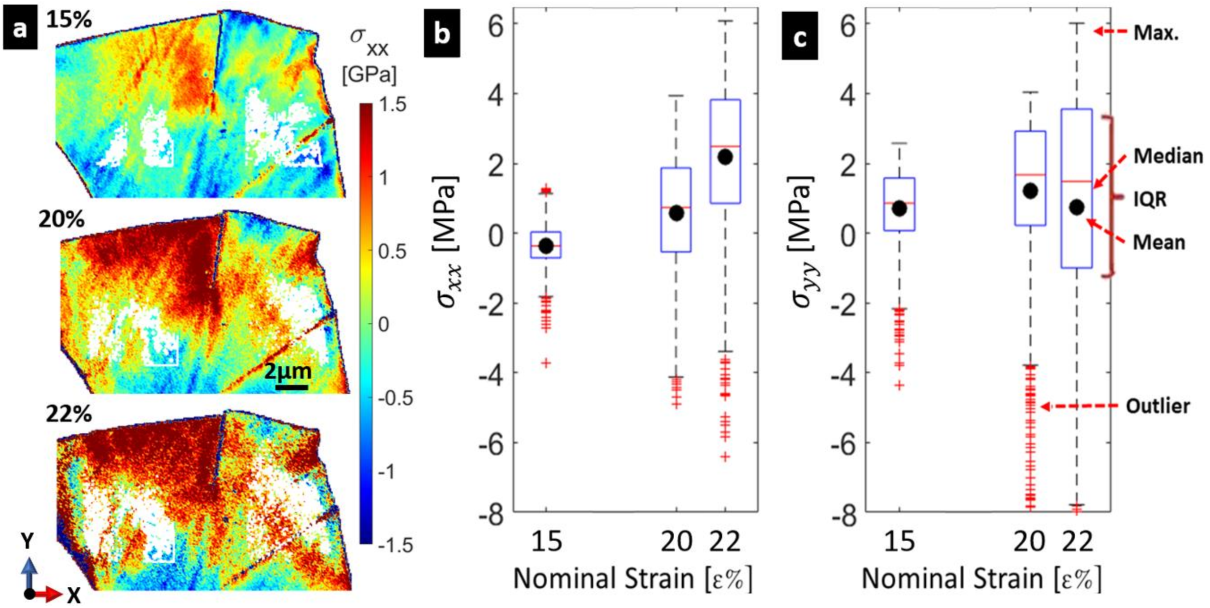

Figure 8: Maps of σ_{xx} in grain (α,2) at nominal strains of 15% to 22%, obtained using the chosen reference pattern at 15% strain. The white regions show where data for the background stresses have been selected that are remote from stress concentrations (see main text for criteria). The orthogonal stresses σ_{xx} (parallel to loading) and σ_{yy} (perpendicular to loading) are plotted in b) and c), where the mean, median, interquartile range (IQR) are shown. Outliers are identified as values 1.5 times more than the interquartile range.

3.4. *J*-integral Analysis

To simplify the *J*-integral analysis, the elastic strain field (ε) at the tip of the deformation twin (white box in Figure 7.b in ε_{xy}) was transformed to a new reference frame (ε') using a 2D rotation matrix, so the twin trace was parallel to the horizontal x axis of the new coordinate frame. The elastic nodal displacement field in the new coordinate system was computed by integrating the measured elastic strain field (one datum per EBSD measurement point). This employed a method implemented in MATLAB to create a uniform rectangular grid with 4 nodes (equivalent to a CPS4 element in ABAQUS®) around each element, with 4 Gaussian points (full Gaussian quadrature integration) per element to increase integration accuracy [77]. The remaining 2D (planar) rigid body motions (translations and a 0.01° rotation) were then removed from the integrated displacement field, selecting the point with absolute minimum displacement as the origin [78]. Figure 9 shows, at each level of applied strain, the field of the integrated displacement magnitude (after rotation and rigid body motion correction).

Using a MATLAB code[1], these nodal displacements were injected into the ABAQUS® finite element solver as boundary conditions, which applied an anisotropic linear elastic model (ferrite elastic constants) oriented to the crystal frame of reference (See Supplementary Information B). The ABAQUS® solver was used to calculate the *J*-integral (treating the twin as a traction free interface) assuming plane stress conditions. The Mode-I and II stress intensity factors (SIF), K_I and K_{II}, were then obtained using the interaction integral method that is implemented natively in ABAQUS® [44], [79]. In this analysis, the equivalent domain integral (EDI) [80] was defined by an inner contour that enclosed the twin-tip and outer contours that expanded outwards (in intervals of 3 nodes).

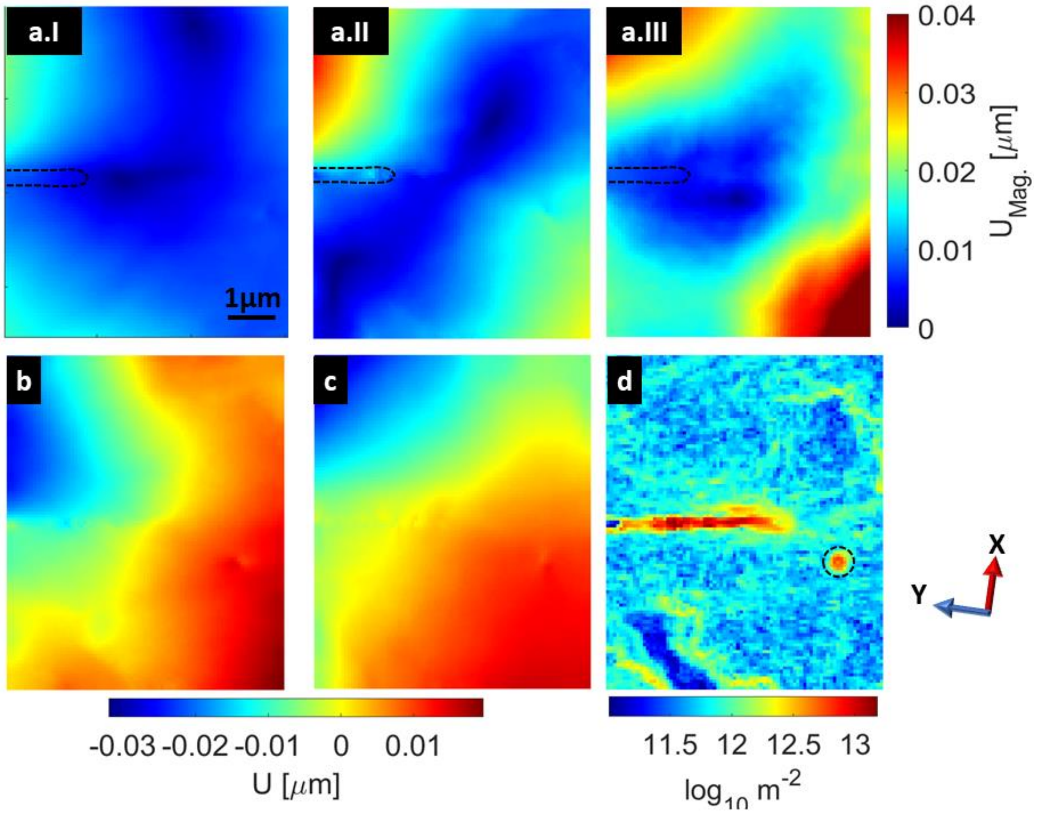

Figure 9: (a) Integrated displacement field (displacement magnitude) around the twin-tip (dashed black lines) at applied nominal strains of I) 15%, II) 20% and III) 22%. Integrated (b) Ux, (c) Uy and (d) GND density at 20% applied nominal strain. The axes X and Y are the parallel to those in Figure 7.

The *J*-integral analysis is only valid (path independent) under small scale yielding conditions where excessive plasticity is not present [81], [82]. In principle, convergence of the J-integral may be achieved in the region of plastic deformation (i.e. the HRR (Hutchinson [83], and Rice

---

[1] https://bit.ly/3qfEPdY

and Rosengren [84]) singularity), and beyond where linear elastic behaviour dominates. Inaccurate knowledge of twin tip location would influence the convergence [85]–[87], but the tip location was quite precisely located as shown in Figure 6. Non-convergence near the twin tip is observed in all the analyses particularly in regions of high GND (Figure 9.d). The presented values of the J-integral and the K_I and K_{II} SIFS are the converged results. This is illustrated in Figure 10, where the evolution of the *J*-integral as the contour expands from the twin-tip is shown for each applied strain. The *J*-integral stabilises with increasing domain size, and the stable value was evaluated using the mean and the variance of the mean over all the contours from the 11th (i.e. beyond approximately 1.3 µm from the twin tip) as highlighted in Figure 10a. The maximum number of contours (or domain size) was restricted to 22 (approximately 2.6 µm) as further extension of the domain reduced the stability of the convergence due to adjacence to other strain concentrators such as a $(2\bar{1}\bar{1})[\bar{1}\bar{1}\bar{1}]$ slip-band. Table 1 summarises the average *J*-integral, together with the mode I and II SIFs (K_I and K_{II}). The values of twin thickness (calculated from the surface width using the twin orientation relative to the surface [88]) and length, correlation peak height (PH), mean angular error (MAE), and the density of geometrically necessary dislocations (GND) evaluated within the displacement integration window are also presented in Table 1.

The *J*-integral increased with applied strain between the 1st and 2nd observation stages (15% and 20% strain) and then did not change significantly in the 3rd stage (22% strain). The twin thickness increased significantly only between the 1st and 2nd stage. Overall, the twin length increased slightly by approximately 40 nm, from an initial length of ~5.6 µm. The mean angular error (MAE) of the EBSPs in the displacement integration window increased significantly in the 3rd observation, with a corresponding decrease in correlation peak height (PH) (Figure 10b). This was judged to be due to contamination from deposited carbon caused by electron-beam-induced decomposition of gaseous hydrocarbons, which can accumulate during the EBSD scan [89]. The effect of this deposition can be seen in contour 13 (approx. 1.5 µm from the twin tip) for the 1st observation (Figure 10a), which coincide with the visible carbon deposition in the FSD image (Figure 5a and Figure 9.d). As the integration domain expands, it becomes less sensitive to local errors in the displacement field. Nonetheless, the increase in contamination at the 3rd observation increased the noise in the displacement field and increased the uncertainty in the *J*-integral. The mode I SIF (K_I) increased with applied strain, whereas the mode II SIF (K_{II}) was approximately constant and then increased in the 3rd observation at 22% applied strain (Table 1). The mean GND density value was calculated inside the integration window (Figure 9) while excluding non-indexed regions from the EBSD map. This GND density increased by a factor of ~3 (i.e. 0.50 ± 0.16 $\log_{10}$ m^{-2}) between the first and second observation, and by a factor of ~6 (i.e. 0.8 ± 0.14 $\log_{10}$ m^{-2}) between the second and third observations.

Table 1: Summary of the numerical results for in situ observation of the twin, as a function of nominal applied strain.

Nom. Strain %	Twin Thickness (nm)	Twin Length (nm)	*J* (J m^{-2})	K_I (MPa m$^{1/2}$)	K_{II} (MPa m$^{1/2}$)	GND ($\log_{10}$ m^{-2})	PH	MAE (10^{-4} rad)
15	401 ± 11	5630 ± 12	3.6 ± 0.3	0.47 ± 0.09	0.66 ± 0.03	11.5 ± 0.11	0.78 ± 0.01	0.8 ± 0.3
20	710 ± 19	5678 ± 6	11.1 ± 0.9	2.71 ± 0.11	0.60 ± 0.14	11.9 ± 0.12	0.69 ± 0.01	2.5 ± 0.8
22	736 ± 12	5690 ± 6	11.0 ± 1.3	3.25 ± 0.16	1.93 ± 0.14	12.7 ± 0.08	0.57 ± 0.04	8.2 ± 1.8

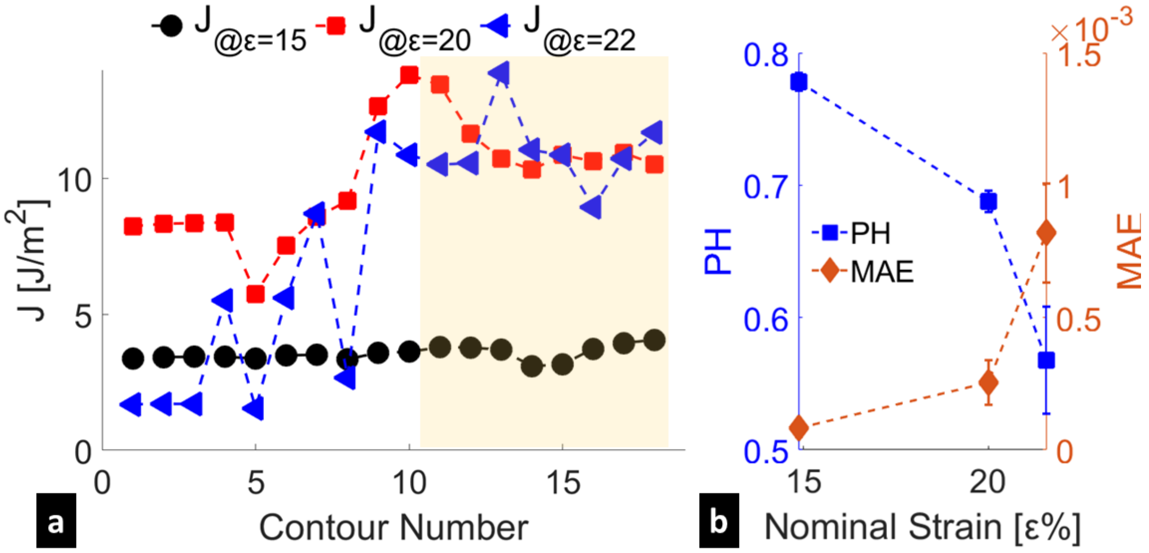

Figure 10: (A) Strain energy release rate (*J*-integral) with contour number at nominal strains of 15, 22 and 25%. (B) Mean angular error (MAE) and cross-correlation peak height (PH) as a function of the applied nominal strain.

3.5. Ex Situ Analysis of Ferrite Deformation Twins

A ROI was identified in an unloaded specimen with three deformation twins of different thickness within the same ferrite grain (Figure 11a). HR-EBSD maps of the stress field (Figure 11b) were calculated relative to the least deformed reference pattern ($EBSP_0$) in the map. The twins, identified by trace analysis as $\sum 3\ (\bar{1}2\bar{1})[\bar{1}\bar{1}\bar{1}]$, have their tips within the grain, with twin habit plane inclined at 33° to the surface of the specimen. The projection of the twin shear direction is at 77° to the applied loading (X_{twin} in Figure 11a). The twin thickness was obtained from the measured surface width and twin plane orientation, as the in situ test.

Analysis of the *J*-integral for each twin was performed following rotation of the HR-EBSD data and its integration to the displacement field. As for the in situ analysis, the number of contours (or domain size) was limited to a domain where stable convergence was achieved. The analysis found an increase in J from 5.04 ± 0.07 J m^{-2} to 8.29 ± 0.98 J m^{-2} with increasing twin thickness (Figure 11c). Decomposition of the J-integral into mode I and mode II SIFs (K_I and K_{II}) shows an increase in K_I with increasing twin thickness (from 1.03 ± 0.01 to 1.43 ± 0.08 MPa $m^{1/2}$). Both K_{II} and the density of GNDs are small and nearly constant with twin thickness; between -0.01 ± 0.00 to 0.04 ± 0.01 MPa $m^{1/2}$, and between 11.98 ± 0.22 to 12.17 ± 0.19 $\log_{10}$ m^{-2}, respectively.

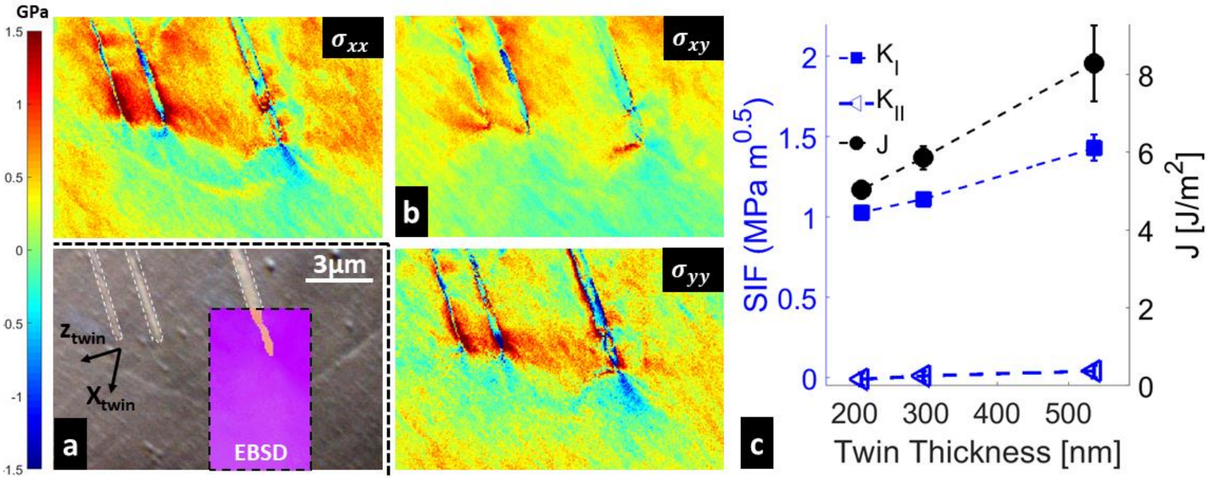

Figure 11: a) FSD image (with inset EBSD map of grain orientation) of three $\sum 3\ (\bar{1}2\bar{1})[\bar{1}\bar{1}\bar{1}]$ ferrite deformation twins in age hardened duplex stainless-steel. b) HR-EBSD calculated stress tensors. c) *J*-integral, and Mode-I and II stress intensity factors (K_I and K_{II}) as a function of twin thickness. Strains calculated using the least deformed reference pattern ($EBSP_0$) with mean MAE value of $3.5 \pm 0.6 \times 10^{-4}$ rad and PH of 0.86 ± 0.02.

The J-integral obtained from ex situ observations of other intragranular twins that were analysed by the same method are summarised in Figure 12. Details of the twins (e.g. orientations, width, thickness (i.e. calculated using the angle between the twin plane and surface, etc) are given in Supplementary Information: D. The SIFs were also decomposed from the J-integral. The values of K_{II} is generally small for all twins, with no systematic relationship to the value of the J-integral. No relation was found also between the mode II SIF and the orientation of the twin (e.g. orientation of the twin plane normal and shear direction relative to the observed surface). There is a quite good correlation between K_I and the square root of the *J*-integral (Figure 12) since for small K_{II} the strain energy field is dominated by K_I.

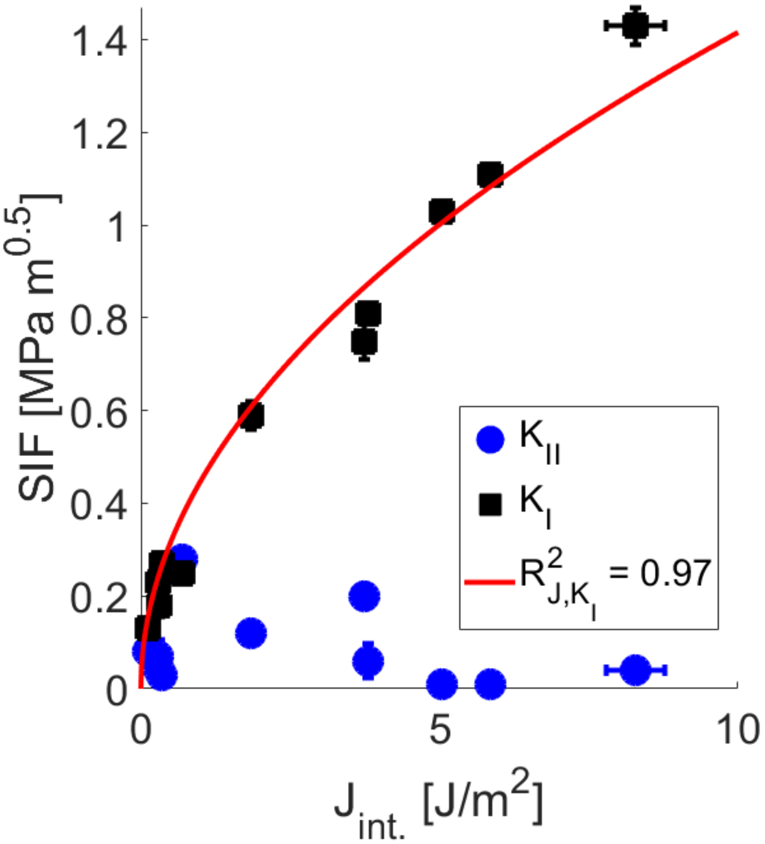

Figure 12: The J-integral and decomposed stress intensity factors (SIF, K_I and K_{II}) obtained by analysis of HR-EBSD measurements of the elastic strain field ahead of intragranular ferrite deformation twins in different grains, observed ex-situ with no loading. The fitted relationship is $K_I = \sqrt{0.2J}$ for K in MPa $m^{0.5}$ and J in Jm^{-2}.

4. Discussion

The in situ analysis focused on a ferrite grain in which a deformation twin propagated slightly as the load was increased, and thickened noticeably (Figure 6c). The thickening of the twin was accompanied by thickening of the slip band that was associated with the twin. This indicates that the two features were interacting as the grains deformed under the applied tensile strain. The average change measured in the background stress in the ROI, parallel to the applied remote tensile loading, was approximately 2.6 MPa (Figure 8b), which is small compared to the change in applied tensile stress of 72.5 MPa (Figure 4a). The points used to calculate Figure 8b and 8c were selected to be remote from stress concentrations (Figure 8a) for the purpose of monitoring the response of the background stress to tensile loading and to verify the set-up stability as correlated changes in σ_{xx} and σ_{yy} would indicate sample movement. Systematic bias might arise from microscope stability issues or sample movement, and could induce errors of up to 10^{-3} strain [90] (i.e. ~200 MPa). A smaller bias might arise from changes in EBSP acquisition configuration (between observations) that would be induced by surface movements due to sample necking. However, this would be expected to affect both stress components similarly. The observed increase in mean background σ_{xx} with negligible change in mean background σ_{yy} shows the tensile background stress increased with increasing applied tensile strain. The significant difference between the increase in mean background σ_{xx} and the applied stress may be due to the heterogeneous deformation of the polygranular microstructure. Large differences have been reported previously between the average stress in a plastically-yielding grain and the average stress on a polycrystalline bulk sample [91], [92]. The high levels of stress at grain boundaries (Figure 8a) show the average stress on the grain is much higher than the background stress. Strain hardening in duplex stainless steel occurs primarily in the austenite phase [93], and this will also play a role of reducing the stress carried by ferrite grains.

The in situ study finds that the mode-I SIF increased with twin thickness. The mode-II SIF did not change significantly between the 1st and 2nd observations but increased substantially in the 3rd observation. There was a corresponding increase in the mean GND density ahead of the twin by a factor of 3 between the first and second observation, and by a larger factor of 6.3 between the second and third observations. The GND should be considered as the lower-limit of plasticity since EBSD cannot probe the total dislocation density that includes the statistically-stored dislocations. The increased GND density indicates an increase of the plastic deformation ahead of the twin-tip, and this would be consistent with the shear strain of twin growth [94], [95]. The twin shear direction is not parallel to the trace of the twin, but the shear deformation in the plane of the analysed surface is represented by K_{II}, which increases correspondingly. The current 2D analysis may lack sufficient sensitivity to detect the change in K_{II} between the 1st and 2nd observations.

The ex situ observation of twins of the same orientation within the same grain also reveals a strong correlation between K_I and twin thickness (Figure 11c). The ex situ values of K_{II} are small in comparison to the in situ study. Low values of K_{II} indicate that the twin shear has been relaxed by the removal of the mechanical load, leading to elastic recovery of the surrounding grain (Figure 12). However, de-twinning is prevented by the pinning effect of the residual dislocations at the twin-parent boundaries [96]. The mode I stress intensity factor, K_I, which dominates the description of the strain field when K_{II} is small, is also expected to be decreased by the removal of the applied load.

The difficulty of detailed interpretation of these two-dimensional results is apparent and we will not attempt to use this analysis to reconcile current ideas about twin propagation in BCC materials (e.g. [97], [98]). The limitations are mainly because the current 2D analysis provides only a semi-quantitative assessment of the 3D deformation field. For instance, differences between the measured fields of twins of different orientation cannot be quantified using the current analysis; for an inclined twin plane, where the twin out-of-plane shear is significant, this shear will contribute to the KI field that is measured in a 2D analysis [99]. Nonetheless, the observations are consistent with the simulations that the stress field of twins is related to their ellipsoidal shape, and that the magnitude of the stress concentration increases with twin thickness [18].

The significant difference in the magnitude of the elastic fields from in situ and ex situ observations shows that ex situ analysis of unloaded material does not measure the conditions that pertain at the tip of a propagating twin, and so cannot quantify the criterion for twin propagation. In situ analysis methods, such as HR-EBSD, are required that can quantify the critical elastic strain field around the twin as it propagates, and the plasticity also. The 2D analysis methodology presented here could be applied to investigate the criterion for twin growth in observations of carefully selected twins (e.g. where the twin shear is parallel to the surface). Twins of more general orientations, with a similar 3D analysis of the elastic strain field, might be examined using a technique such as Laue microdiffraction that unlike HR-EBSD also has the advantage of absolute strain measurement [100]–[103].

It is worth noting that the crack-like *J*-integral analysis strictly requires the contour to start and end from a traction-free surface, and therefore does not consider any internal pressure that might be exerted at the twin-parent boundary. Thus, to maintain the path independence of the integral, the *J*-integral definition of the contour path should be extended to include the twin-parent boundary [104] (similar to hydraulic fracture [105]), as described by the 2nd term of equation (3) where f^c is the twin surface (Γ_c) traction vector.

$$J = \int_{\Gamma} \left(W dx_2 - T_i \frac{\partial u_i}{\partial x_1} ds \right) - \int_{\Gamma_c} \mathrm{f}^c \frac{\partial u_i}{\partial x_1} ds \tag{3}$$

The mechanism for the lateral expansion of twins remains a topic of debate [106] and there no available three-dimensional models for twin propagation that relate the twin-tip morphology to twin propagation and thickening [27], and the interaction between the residual dislocations at twin-parent grain boundary during thickening [33] expressed as an explicit force, i.e. f^c. Recently, an iterative model has been suggested. This method assumes a linear proportionality of stress at the interface to the twin thickness with a potential energy barrier as the rate-determining step [95], [107]. For the current in situ analysis, it is judged there is a minimal effect of neglecting f^c on the path independency. As for the ex situ analysis, removal of the load leaves the twin-parent grain boundary in an equilibrium state with no force available for twin thickening or detwinning (i.e. f^c=0).

This work has measured the local stress state surrounding the tips of deformation twins by HR-EBSD. The present measurement is relative rather than absolute since the strain field depends on the reference pattern (EBSP_0); an objective method has been proposed for the selection of the reference pattern with the least strain. We have shown that the mechanical conditions can be further parameterised by decomposition of the strain energy release rate that is directly calculated via *J*-integral analysis. There are arguments for the insufficiency of an elastic field-based criterion (i.e. energy release rate) for twin nucleation and growth, and criteria for stored (dislocation structure) energy have been recently proposed [108], [109]. Indeed, the local field in the immediate vicinity of the twin-tip is complicated by plastic deformation. However, the *J*-integral analysis describes the elastic strain field in the wider envelope of material that acts on the twin tip. This field mediates between the applied remote loading and twin propagation to provide a local boundary description of the critical conditions, and knowledge of this can be used to inform more detailed modelling. The conservation integrals treatment (as amplified by Eshelby [36]) is also direct and simple, without the need for fitting approaches that are based on assumed fields. This study considered the ferrite phase of the duplex stainless steel in only one condition of age-hardening, caused by spinodal decomposition. Further studies with analysis of the strain fields associated with the propagation and thickening of twins in the ferrite as a function of ageing conditions might elucidate whether the transition that occurs from spinodal decomposition to precipitation at higher temperatures and longer aging times [110] influences twin development.

In summary, we propose that the *J*-integral can be used as an approximate descriptor of the characteristic deformation field at the tip of a twin, by treating the twin as a discontinuity. Ultimately, volumetric quantification by this approach may provide insights into criteria for twin propagation, thickening and variant selection. The method is of interest because, firstly, the *J*-integral can be calculated directly from experimental data, without the need to resort to crystal plasticity models and without knowledge of the loading condition or specimen geometry. Secondly, the mechanical condition ahead of a twin can be readily obtained by decomposing the *J*-integral into opening and shear modes that can be described as stress intensity factors. Thirdly, the nature of *J*-integral facilitates the employment of finite element (FE) analysis, and its evaluation is implemented natively in most FE solvers. Furthermore, the experimental strain-integrated displacement field that is used in the evaluation of the *J*-integral can be easily incorporated with crystal plasticity models, which can simulate twin growth via the extended finite element method (XFEM [111], [112]). Such analyses would benefit from advanced strain energy integral definitions that can address factors including surface traction [104], thermal and residual stresses [113] and boundary interactions [114], [115], which are natively implemented in commercial Finite element software.

5. Conclusion

The strain fields ahead of ferrite deformation twins have been quantified in a study of the ferrite matrix of Zeron 100 duplex stainless steel (DSS), which was age hardened for 100 hours then deformed in tension and characterised in situ and ex situ by high-resolution electron backscatter diffraction (HR-EBSD). An improved method for reference pattern ($EBSP_0$) selection was applied that utilised the inverse relationship between the cross-correlation peak height (PH) and the square-root of the mean angular error (MAE) with PH.

For the first time, the elastic strain field surrounding the twin-tip was integrated into a 2D displacement field and injected in a plane stress finite element simulation (ABAQUS®) to calculate the elastic strain energy release rate (*J*-integral), which was then decomposed into mode-I and mode-II stress intensity factors.

As perceived from these surface measurements, the strain field described by the mode-I stress intensity factor increased with twin thickness. This is judged to be in order to accommodate the dimensional change of the ellipsoidal twin. The strain field, shown particularly by the in-plane shear mode II stress intensity factor, relaxed significantly when unloaded in the ex situ studies, compared to the in situ case.

Declaration of Competing Interest

The authors declare that they have no known competing financial interests or personal relationships that could have appeared to influence the work reported in this paper.

Acknowledgements

The authors would like to thank Dr Roger Francis (Rolled Alloys www.rolledalloys.com) for supplying the specimen material, Ms Marzena Tkaczyk (Laboratory for In-situ Microscopy and Analysis, LIMA) for her guidance and help with the experiment, and Dr Phani Karamched (Oxford Micromechanics Group, OMG) for insightful discussions about HR-EBSD and plasma cleaning. The authors acknowledge the use of characterisation facilities within the David Cockayne Centre for Electron Microscopy (DCCEM), Department of Materials, University of Oxford, alongside financial support provided by the Henry Royce Institute (Grant ref

EP/R010145/1). Abdalrhaman Koko is supported by an EPSRC Engineering research studentship (Grant ref EP/N509711/1).

Authorship Contribution Statement

Abdalrhaman Koko: Conceptualization, Methodology, Software, Investigation, Formal analysis, Writing - original draft, Visualization.

Elsiddig Elmukashfi: Software.

Kalin Dragnevski: Resources.

Angus J. Wilkinson: Software, Writing - review & editing.

Thomas James Marrow: Conceptualization, Methodology, Writing - review & editing, Supervision, Funding Acquisition.

References

[1] J. W. Christian and S. Mahajan, "Deformation twinning," *Prog. Mater. Sci.*, vol. 39, no. 1–2, pp. 1–157, Jan. 1995.

[2] B. A. Bilby, A. G. Crocker, and A. H. Cottrell, "The theory of the crystallography of deformation twinning," *Proc. R. Soc. London. Ser. A. Math. Phys. Sci.*, vol. 288, no. 1413, pp. 240–255, Oct. 1965.

[3] J. A. Venables, "Deformation twinning in face-centred cubic metals," *Philos. Mag. A J. Theor. Exp. Appl. Phys.*, vol. 6, no. 63, pp. 379–396, Mar. 1961.

[4] J. W. Christian, "Deformation Twinning," in *The Theory of Transformations in Metals and Alloys*, Elsevier, 2002, pp. 859–960.

[5] J. A. Venables, "The nucleation and propagation of deformation twins," *J. Phys. Chem. Solids*, vol. 25, no. 7, pp. 693–700, 1964.

[6] S. Mahajan and D. F. Williams, "Deformation Twinning in Metals and Alloys," *Int. Metall. Rev.*, vol. 18, no. 2, pp. 43–61, Jun. 1973.

[7] A. Kauffmann *et al.*, “Severe deformation twinning in pure copper by cryogenic wire drawing,” *Acta Mater.*, vol. 59, no. 20, pp. 7816–7823, Dec. 2011.

[8] S. G. Song and G. T. Gray, “Structural interpretation of the nucleation and growth of deformation twins in Zr and Ti—I. Application of the coincidence site lattice (CSL) theory to twinning problems in h.c.p. structures,” *Acta Metall. Mater.*, vol. 43, no. 6, pp. 2325–2337, 1995.

[9] J. Johansson and M. Odén, “Load sharing between austenite and ferrite in a duplex stainless steel during cyclic loading,” *Metall. Mater. Trans. A*, vol. 31, no. 6, pp. 1557–1570, 2000.

[10] T. J. Marrow and J. E. King, “Fatigue crack propagation mechanisms in a thermally aged duplex stainless steel,” *Mater. Sci. Eng. A*, vol. 183, no. 1, pp. 91–101, 1994.

[11] T. J. Marrow, “The fracture mechanism in 475°C embrittled ferritic stainless steels,” *Fatigue Fract. Eng. Mater. Struct.*, vol. 19, no. 7, pp. 919–933, Jul. 1996.

[12] C. N. Reid, “The association of twinning and fracture in bcc metals,” *Metall. Trans. A*, vol. 12, no. 3, pp. 371–377, 1981.

[13] T. J. Marrow and C. Harris, “The fracture mechanism of 475°C embrittlement in a duplex stainless steel,” *Fatigue Fract. Eng. Mater. Struct.*, vol. 19, no. 7, pp. 935–947, Jul. 1996.

[14] R. W. Cahn, “Twinned crystals,” *Adv. Phys.*, vol. 3, no. 12, pp. 363–445, Oct. 1954.

[15] S. Wang *et al.*, “Variant selection criterion for twin variants in titanium alloys deformed by rolling,” *Acta Mater.*, vol. 60, no. 9, pp. 3912–3919, May 2012.

[16] B. Li, H. El Kadiri, and M. F. Horstemeyer, “Extended zonal dislocations mediating twinning in titanium,” *Philos. Mag.*, vol. 92, no. 8, pp. 1006–1022, Mar. 2012.

[17] T. B. Britton, F. P. E. Dunne, and A. J. Wilkinson, “On the mechanistic basis of deformation at the microscale in hexagonal close-packed metals,” *Proc. R. Soc. A Math. Phys. Eng. Sci.*, vol. 471, no. 2178, p. 20140881, Jun. 2015.

[18] Y. Paudel, C. D. Barrett, M. A. Tschopp, K. Inal, and H. El Kadiri, “Beyond initial twin nucleation in hcp metals: Micromechanical formulation for determining twin spacing during deformation,” *Acta Mater.*, vol. 133, pp. 134–146, 2017.

[19] H. Mughrabi, “Dislocation wall and cell structures and long-range internal stresses in deformed metal crystals,” *Acta Metall.*, vol. 31, no. 9, pp. 1367–1379, Sep. 1983.

[20] I. J. Beyerlein, X. Zhang, and A. Misra, “Growth Twins and Deformation Twins in Metals,” *Annu. Rev. Mater. Res.*, vol. 44, no. 1, pp. 329–363, Jul. 2014.

[21] I. A. O. and A. G. Sheinerman, “Nanoscale cracks at deformation twins stopped by grain boundaries in bulk and thin-film materials with nanocrystalline and ultrafine-grained structures,” *J. Phys. D. Appl. Phys.*, vol. 47, no. 1, p. 15307, 2014.

[22] Y. Zhang, N. R. Tao, and K. Lu, “Effect of stacking-fault energy on deformation twin thickness in Cu–Al alloys,” *Scr. Mater.*, vol. 60, no. 4, pp. 211–213, 2009.

[23] I. J. Beyerlein, L. Capolungo, P. E. Marshall, R. J. McCabe, and C. N. Tomé, “Statistical analyses of deformation twinning in magnesium,” *Philos. Mag.*, vol. 90, no. 16, pp. 2161–2190, 2010.

[24] A. W. Sleeswyk, “Emissary dislocations: Theory and experiments on the propagation of deformation twins in α-iron,” *Acta Metall.*, vol. 10, no. 8, pp. 705–725, 1962.

[25] J. Spreadborough, D. Langheinrich, E. Anderson, and D. Brandon, “Etch-Pit Observations Concerning Twins in Iron and Iron Alloys,” *J. Appl. Phys.*, vol. 35, no. 12, pp. 3585–3587, Dec. 1964.

[26] H. Abdolvand and A. J. Wilkinson, “Assessment of residual stress fields at deformation twin tips and the surrounding environments,” *Acta Mater.*, vol. 105, pp. 219–231, Feb. 2016.

[27] Y. Guo, “The interactions between slip band, deformation twins and grain boundaries in commercial purity titanium,” University of Oxford, 2015.

[28] Y. Guo, H. Abdolvand, T. B. Britton, and A. J. Wilkinson, “Growth of {112¯2} twins in

titanium: A combined experimental and modelling investigation of the local state of deformation,” *Acta Mater.*, vol. 126, pp. 221–235, Mar. 2017.

[29] K. P. Baxevanakis, P. A. Gourgiotis, and H. G. Georgiadis, “Interaction of cracks with dislocations in couple-stress elasticity. Part I: Opening mode,” *Int. J. Solids Struct.*, vol. 118–119, pp. 179–191, Jul. 2017.

[30] J. Kacher, J. E. Sabisch, and A. M. Minor, “Statistical analysis of twin/grain boundary interactions in pure rhenium,” *Acta Mater.*, Apr. 2019.

[31] K. P. D. Lagerlöf, J. Castaing, P. Pirouz, and A. H. Heuer, “Nucleation and growth of deformation twins: A perspective based on the double-cross-slip mechanism of deformation twinning,” *Philos. Mag. A*, vol. 82, no. 15, pp. 2841–2854, Oct. 2002.

[32] M. Gong, J. P. Hirth, Y. Liu, Y. Shen, and J. Wang, “Interface structures and twinning mechanisms of twins in hexagonal metals,” *Mater. Res. Lett.*, vol. 5, no. 7, pp. 449–464, Nov. 2017.

[33] J. T. Lloyd, “A dislocation-based model for twin growth within and across grains,” *Proc. R. Soc. A Math. Phys. Eng. Sci.*, vol. 474, no. 2210, p. 20170709, Feb. 2018.

[34] Y. Wang and J. Li, “Phase field modeling of defects and deformation,” *Acta Mater.*, vol. 58, no. 4, pp. 1212–1235, 2010.

[35] J. D. Eshelby, “The force on an elastic singularity,” *Philos. Trans. R. Soc. London. Ser. A, Math. Phys. Sci.*, vol. 244, no. 877, pp. 87–112, Nov. 1951.

[36] J. D. Eshelby and R. E. Peierls, “The determination of the elastic field of an ellipsoidal inclusion, and related problems,” *Proc. R. Soc. London. Ser. A. Math. Phys. Sci.*, vol. 241, no. 1226, pp. 376–396, Aug. 1957.

[37] J. R. Rice, “A Path Independent Integral and the Approximate Analysis of Strain Concentration by Notches and Cracks,” *J. Appl. Mech.*, vol. 35, no. 2, pp. 379–386, Jun. 1968.

[38] D. M. Parks, “The virtual crack extension method for nonlinear material behavior,”

Comput. Methods Appl. Mech. Eng., vol. 12, no. 3, pp. 353–364, Dec. 1977.

[39] T. H. Becker, M. Mostafavi, R. B. Tait, and T. J. Marrow, “An approach to calculate the J-integral by digital image correlation displacement field measurement,” *Fatigue Fract. Eng. Mater. Struct.*, vol. 35, no. 10, pp. 971–984, Oct. 2012.

[40] S. M. Barhli, M. Mostafavi, A. F. Cinar, D. Hollis, and T. J. Marrow, “J-Integral Calculation by Finite Element Processing of Measured Full-Field Surface Displacements,” *Exp. Mech.*, vol. 57, no. 6, pp. 997–1009, 2017.

[41] S. M. Barhli *et al.*, “Obtaining the J-integral by diffraction-based crack-field strain mapping,” *Procedia Struct. Integr.*, vol. 2, pp. 2519–2526, Jan. 2016.

[42] S. M. Barhli *et al.*, “Synchrotron X-ray characterization of crack strain fields in polygranular graphite,” *Carbon N. Y.*, vol. 124, pp. 357–371, Nov. 2017.

[43] A. Koko, P. Earp, T. Wigger, J. Tong, and T. J. Marrow, “J-integral analysis: An EDXD and DIC comparative study for a fatigue crack,” *Int. J. Fatigue*, vol. 134, p. 105474, May 2020.

[44] C. F. Shih and R. J. Asaro, “Elastic-Plastic Analysis of Cracks on Bimaterial Interfaces: Part I—Small Scale Yielding,” *J. Appl. Mech.*, vol. 55, no. 2, pp. 299–316, Jun. 1988.

[45] X. Jin, J. Wade-Zhu, Y. Chen, P. M. Mummery, X. Fan, and T. J. Marrow, “Assessment of the fracture toughness of neutron-irradiated nuclear graphite by 3D analysis of the crack displacement field,” *Carbon N. Y.*, vol. 171, pp. 882–893, 2021.

[46] T. Benjamin Britton and A. J. Wilkinson, “Stress fields and geometrically necessary dislocation density distributions near the head of a blocked slip band,” *Acta Mater.*, vol. 60, no. 16, pp. 5773–5782, Sep. 2012.

[47] Y. Guo, T. B. Britton, and A. J. Wilkinson, “Slip band–grain boundary interactions in commercial-purity titanium,” *Acta Mater.*, vol. 76, pp. 1–12, Sep. 2014.

[48] J. C. Stinville, N. Vanderesse, F. Bridier, P. Bocher, and T. M. Pollock, “High resolution mapping of strain localization near twin boundaries in a nickel-based superalloy,” *Acta*

Mater., vol. 98, pp. 29–42, 2015.

[49] P. D. Earp, S. M. Barhli, and T. J. Marrow, "Full-field characterisation of the stress concentration of blocked twins by high-resolution EBSD in alpha-uranium," in *ICF 2017 - 14th International Conference on Fracture*, 2017, vol. 2, pp. 128–129.

[50] T. J. Godfrey and G. D. W. Smith, "The Atom Probe Analysis of a Cast Duplex Stainless Steel," *Le J. Phys. Colloq.*, vol. 47, no. C7, pp. C7-217-C7-222, Nov. 1986.

[51] T. J. Marrow, A. O. Humphreys, and M. Strangwood, "The Crack Initiation Toughness for Brittle Fracture of Super Duplex Stainless Steel," *Fatigue Fract. Eng. Mater. Struct.*, vol. 20, no. 7, pp. 1005–1014, Jul. 1997.

[52] C. Örnek, M. G. Burke, T. Hashimoto, and D. L. Engelberg, "748 K (475 °C) Embrittlement of Duplex Stainless Steel: Effect on Microstructure and Fracture Behavior," *Metall. Mater. Trans. A*, vol. 48, no. 4, pp. 1653–1665, 2017.

[53] A. J. Wilkinson and D. Randman, "Determination of elastic strain fields and geometrically necessary dislocation distributions near nanoindents using electron back scatter diffraction," *Philos. Mag.*, vol. 90, no. 9, pp. 1159–1177, Mar. 2010.

[54] J. Jiang, T. B. Britton, and A. J. Wilkinson, "Measurement of geometrically necessary dislocation density with high resolution electron backscatter diffraction: Effects of detector binning and step size," *Ultramicroscopy*, vol. 125, pp. 1–9, Feb. 2013.

[55] J. Luster and M. A. Morris, "Compatibility of deformation in two-phase Ti-Al alloys: Dependence on microstructure and orientation relationships," *Metall. Mater. Trans. A*, vol. 26, no. 7, pp. 1745–1756, 1995.

[56] F. Roters, P. Eisenlohr, L. Hantcherli, D. D. Tjahjanto, T. R. Bieler, and D. Raabe, "Overview of constitutive laws, kinematics, homogenization and multiscale methods in crystal plasticity finite-element modeling: Theory, experiments, applications," *Acta Mater.*, vol. 58, no. 4, pp. 1152–1211, 2010.

[57] T. R. Bieler *et al.*, "The role of heterogeneous deformation on damage nucleation at grain boundaries in single phase metals," *Int. J. Plast.*, vol. 25, no. 9, pp. 1655–1683,

2009.

[58] G. I. Taylor, “The mechanism of plastic deformation of crystals. Part I.—Theoretical,” *Proc. R. Soc. London. Ser. A*, vol. 145, no. 855, pp. 362 LP – 387, Jul. 1934.

[59] G. I. Taylor, “Plastic Strain in Metals,” *Lect. to Inst. Met.*, vol. 62, pp. 307–324, 1938.

[60] C. A. Schneider, W. S. Rasband, and K. W. Eliceiri, “NIH Image to ImageJ: 25 years of image analysis,” *Nat. Methods*, vol. 9, no. 7, pp. 671–675, 2012.

[61] Peter Kovesi, “Image Features from Phase Congruency,” *Videre J. Comput. Vis. Res.*, vol. 1, no. 3, pp. 1–26, 1999.

[62] A. F. Cinar *et al.*, “An autonomous surface discontinuity detection and quantification method by digital image correlation and phase congruency,” *Opt. Lasers Eng.*, vol. 96, pp. 94–106, Sep. 2017.

[63] R. R. Keller, A. Roshko, R. H. Geiss, K. A. Bertness, and T. P. Quinn, “EBSD measurement of strains in GaAs due to oxidation of buried AlGaAs layers,” *Microelectron. Eng.*, vol. 75, no. 1, pp. 96–102, 2004.

[64] S. I. Wright and M. M. Nowell, “EBSD Image Quality Mapping,” *Microsc. Microanal.*, vol. 12, no. 01, pp. 72–84, Feb. 2006.

[65] T. B. Britton and J. L. R. Hickey, “Understanding deformation with high angular resolution electron backscatter diffraction (HR-EBSD),” *IOP Conf. Ser. Mater. Sci. Eng.*, vol. 304, no. 1, p. 12003, 2018.

[66] K. Z. Troost, P. van der Sluis, and D. J. Gravesteijn, “Microscale elastic-strain determination by backscatter Kikuchi diffraction in the scanning electron microscope,” *Appl. Phys. Lett.*, vol. 62, no. 10, pp. 1110–1112, Mar. 1993.

[67] A. J. Wilkinson, G. Meaden, and D. J. Dingley, “High resolution mapping of strains and rotations using electron backscatter diffraction,” *Mater. Sci. Technol.*, vol. 22, no. 11, pp. 1271–1278, Nov. 2006.

[68] J. D. Lord, B. Roebuck, R. Morrell, and T. Lube, “25 year perspective Aspects of strain

and strength measurement in miniaturised testing for engineering metals and ceramics," *Mater. Sci. Technol.*, vol. 26, no. 2, pp. 127–148, Feb. 2010.

[69] T. B. Britton and A. J. Wilkinson, "Measurement of residual elastic strain and lattice rotations with high resolution electron backscatter diffraction," *Ultramicroscopy*, vol. 111, no. 8, pp. 1395–1404, Jul. 2011.

[70] J. Jiang, T. Zhang, F. P. E. Dunne, and T. Ben Britton, "Deformation compatibility in a single crystalline Ni superalloy," *Proc. R. Soc. A Math. Phys. Eng. Sci.*, vol. 472, no. 2185, Jan. 2016.

[71] W. L. Bond, "The Mathematics of the Physical Properties of Crystals," *Bell Syst. Tech. J.*, vol. 22, no. 1, pp. 1–72, Jan. 1943.

[72] T. B. Britton *et al.*, "Tutorial: Crystal orientations and EBSD — Or which way is up?," *Mater. Charact.*, vol. 117, pp. 113–126, Jul. 2016.

[73] S. A. Kim and W. L. Johnson, "Elastic constants and internal friction of martensitic steel, ferritic-pearlitic steel, and α-iron," *Mater. Sci. Eng. A*, vol. 452–453, pp. 633–639, Apr. 2007.

[74] T. B. Britton, V. S. Tong, J. Hickey, A. Foden, and A. J. Wilkinson, "AstroEBSD : exploring new space in pattern indexing with methods launched from an astronomical approach," *J. Appl. Crystallogr.*, vol. 51, no. 6, pp. 1525–1534, Dec. 2018.

[75] S. Sun, B. L. Adams, and W. E. King, "Observations of lattice curvature near the interface of a deformed aluminium bicrystal," *Philos. Mag. A*, vol. 80, no. 1, pp. 9–25, Jan. 2000.

[76] B. . El-Dasher, B. . Adams, and A. . Rollett, "Viewpoint: experimental recovery of geometrically necessary dislocation density in polycrystals," *Scr. Mater.*, vol. 48, no. 2, pp. 141–145, Jan. 2003.

[77] A. Koko, J. Marrow, and E. Elmukashfi, "A Method to Compute the Displacement field from Measured Strain Field," *To Appear*, 2021.

[78] M. Mostafavi *et al.*, "Yield behavior beneath hardness indentations in ductile metals,

measured by three-dimensional computed X-ray tomography and digital volume correlation," *Acta Mater.*, vol. 82, pp. 468–482, 2015.

[79] S. Courtin, C. Gardin, G. Bézine, and H. Ben Hadj Hamouda, "Advantages of the J-integral approach for calculating stress intensity factors when using the commercial finite element software ABAQUS," *Eng. Fract. Mech.*, vol. 72, no. 14, pp. 2174–2185, Sep. 2005.

[80] F. Z. Li, C. F. Shih, and A. Needleman, "A comparison of methods for calculating energy release rates," *Eng. Fract. Mech.*, vol. 21, no. 2, pp. 405–421, 1985.

[81] M. X. Shi, Y. Huang, and H. Gao, "The J-integral and geometrically necessary dislocations in nonuniform plastic deformation," *Int. J. Plast.*, vol. 20, no. 8–9, pp. 1739–1762, Aug. 2004.

[82] J. H. Kuang and Y. C. Chen, "The values of J-integral within the plastic zone," *Eng. Fract. Mech.*, vol. 55, no. 6, pp. 869–881, 1996.

[83] J. W. Hutchinson, "Singular behaviour at the end of a tensile crack in a hardening material," *J. Mech. Phys. Solids*, vol. 16, no. 1, pp. 13–31, Jan. 1968.

[84] J. R. Rice and G. F. Rosengren, "Plane strain deformation near a crack tip in a power-law hardening material," *J. Mech. Phys. Solids*, vol. 16, no. 1, pp. 1–12, Jan. 1968.

[85] S. R. McNeill, W. H. Peters, and M. A. Sutton, "Estimation of stress intensity factor by digital image correlation," *Eng. Fract. Mech.*, vol. 28, no. 1, pp. 101–112, Jan. 1987.

[86] S. Roux and F. Hild, "Stress intensity factor measurements from digital image correlation: post-processing and integrated approaches," *Int. J. Fract.*, vol. 140, no. 1–4, pp. 141–157, Jul. 2006.

[87] S. Yoneyama, Y. Morimoto, and M. Takashi, "Automatic Evaluation of Mixed-mode Stress Intensity Factors Utilizing Digital Image Correlation," *Strain*, vol. 42, no. 1, pp. 21–29, Feb. 2006.

[88] P. E. Marshall, G. Proust, J. T. Rogers, and R. J. McCabe, "Automatic twin statistics from

electron backscattered diffraction data," *J. Microsc.*, vol. 238, no. 3, pp. 218–229, Jun. 2010.

[89] A. J. V Griffiths and T. Walther, "Quantification of carbon contamination under electron beam irradiation in a scanning transmission electron microscope and its suppression by plasma cleaning," *J. Phys. Conf. Ser.*, vol. 241, p. 012017, Jul. 2010.

[90] T. B. Britton *et al.*, "Factors affecting the accuracy of high resolution electron backscatter diffraction when using simulated patterns," *Ultramicroscopy*, vol. 110, no. 12, pp. 1443–1453, Nov. 2010.

[91] B. Clausen, T. Lorentzen, M. A. M. Bourke, and M. R. Daymond, "Lattice strain evolution during uniaxial tensile loading of stainless steel," *Mater. Sci. Eng. A*, vol. 259, no. 1, pp. 17–24, 1999.

[92] K. Chatterjee *et al.*, "Study of grain-level deformation and residual stresses in Ti-7Al under combined bending and tension using high energy diffraction microscopy (HEDM)," *Int. J. Solids Struct.*, vol. 94–95, pp. 35–49, Sep. 2016.

[93] E. Gadalińska *et al.*, "Direct determination of phase stress evolution in duplex steel using synchrotron diffraction," *Mater. Sci. Eng. A*, vol. 801, p. 140355, 2021.

[94] M. A. Meyers, O. Vöhringer, and V. A. Lubarda, "The onset of twinning in metals: a constitutive description," *Acta Mater.*, vol. 49, no. 19, pp. 4025–4039, Nov. 2001.

[95] N. Grilli, A. C. F. Cocks, and E. Tarleton, "A phase field model for the growth and characteristic thickness of deformation-induced twins," *J. Mech. Phys. Solids*, vol. 143, no. 104061, p. 104061, Oct. 2020.

[96] Y. Guo, J. Schwiedrzik, J. Michler, and X. Maeder, "On the nucleation and growth of {112¯2} twin in commercial purity titanium: In situ investigation of the local stress field and dislocation density distribution," *Acta Mater.*, vol. 120, pp. 292–301, 2016.

[97] D.-S. Xu, J.-P. Chang, J. Li, R. Yang, D. Li, and S. Yip, "Dislocation slip or deformation twinning: confining pressure makes a difference," *Mater. Sci. Eng. A*, vol. 387–389, pp. 840–844, 2004.

[98] Y. Gao, Y. Zhang, and Y. Wang, “Determination of twinning path from broken symmetry: A revisit to deformation twinning in bcc metals,” *Acta Mater.*, vol. 196, pp. 280–294, 2020.

[99] Z. He and A. Kotousov, “On Evaluation of Stress Intensity Factor from In-Plane and Transverse Surface Displacements,” *Exp. Mech.*, vol. 56, no. 8, pp. 1385–1393, 2016.

[100] A. A. MacDowell *et al.*, “Submicron X-ray diffraction,” *Nucl. Instruments Methods Phys. Res. Sect. A Accel. Spectrometers, Detect. Assoc. Equip.*, vol. 467–468, pp. 936–943, 2001.

[101] L. Wang, R. Barabash, T. Bieler, W. Liu, and P. Eisenlohr, “Study of {11-21} Twinning in α-Ti by EBSD and Laue Microdiffraction,” *Metall. Mater. Trans. A*, vol. 44, no. 8, pp. 3664–3674, 2013.

[102] Y. Guo *et al.*, “Measurements of stress fields near a grain boundary: Exploring blocked arrays of dislocations in 3D,” *Acta Mater.*, vol. 96, pp. 229–236, Sep. 2015.

[103] Y. Guo, D. M. Collins, E. Tarleton, F. Hofmann, A. J. Wilkinson, and T. Ben Britton, “Dislocation density distribution at slip band-grain boundary intersections,” *Acta Mater.*, vol. 182, pp. 172–183, Jan. 2020.

[104] A. Karlsson and J. Bäcklund, “J-integral at loaded crack surfaces,” *Int. J. Fract.*, vol. 14, no. 6, 1978.

[105] H. Song and S. S. Rahman, “An extended J-integral for evaluating fluid-driven cracks in hydraulic fracturing,” *J. Rock Mech. Geotech. Eng.*, vol. 10, no. 5, pp. 832–843, 2018.

[106] N. Grilli, E. Tarleton, P. D. Edmondson, M. N. Gussev, and A. C. F. Cocks, “In situ measurement and modelling of the growth and length scale of twins in α-uranium,” *Phys. Rev. Mater.*, vol. 4, no. 4, p. 43605, Apr. 2020.

[107] H. Qiao, M. R. Barnett, and P. D. Wu, “Modeling of twin formation, propagation and growth in a Mg single crystal based on crystal plasticity finite element method,” *Int. J. Plast.*, vol. 86, pp. 70–92, 2016.

[108] C. Paramatmuni, Z. Zheng, W. M. Rainforth, and F. P. E. Dunne, “Twin nucleation and variant selection in Mg alloys: An integrated crystal plasticity modelling and experimental approach,” *Int. J. Plast.*, vol. 135, p. 102778, 2020.

[109] D. Wilson, Z. Zheng, and F. P. E. Dunne, “A microstructure-sensitive driving force for crack growth,” *J. Mech. Phys. Solids*, vol. 121, pp. 147–174, 2018.

[110] F. Danoix, P. Auger, and D. Blavette, “Hardening of Aged Duplex Stainless Steels by Spinodal Decomposition,” *Microsc. Microanal.*, vol. 10, no. 3, pp. 349–354, Jun. 2004.

[111] S. Mohammadi, “New Frontiers,” in *Extended Finite Element Method*, S. Mohammadi, Ed. Oxford, UK: Blackwell Publishing Ltd, 2008, pp. 189–217.

[112] E. Giner, N. Sukumar, J. E. Tarancón, and F. J. Fuenmayor, “An Abaqus implementation of the extended finite element method,” *Eng. Fract. Mech.*, vol. 76, no. 3, pp. 347–368, 2009.

[113] C. F. Shih, B. Moran, and T. Nakamura, “Energy release rate along a three-dimensional crack front in a thermally stressed body,” *Int. J. Fract.*, vol. 30, no. 2, pp. 79–102, 1986.

[114] H. Ming-Yuan and J. W. Hutchinson, “Crack deflection at an interface between dissimilar elastic materials,” *Int. J. Solids Struct.*, vol. 25, no. 9, pp. 1053–1067, 1989.

[115] H. Yu, L. Wu, L. Guo, Q. He, and S. Du, “Interaction integral method for the interfacial fracture problems of two nonhomogeneous materials,” *Mech. Mater.*, vol. 42, no. 4, pp. 435–450, 2010.

Supplementary Information

A. Selection Method for Reference Electron Backscatter Pattern (EBSP$_o$)

B. Anisotropic Elastic Stiffness Matrix Rotation

C. Trace Analysis

D. Additional Ex Situ Results

E. Effect of Swapping EBSP$_0$